Three-dimensional time-domain particle-in-cell calculations of impedances and centroid deflections in a linear-accelerator cell

C. Thoma,* D. R. Welch, A. M. Russell, R. E. Clark, and D. V. Rose
Voss Scientific, LLC, Albuquerque, New Mexico 87108, USA

W. A. Stygar
Lawrence Livermore National Laboratory, Livermore, California 94550, USA

B. J. Kelsall
MuEpsln, LLC, Chadds Ford, Pennsylvania 19317, USA

(Received 15 July 2022; accepted 15 December 2022; published 11 January 2023)

In linear induction accelerators, high-brightness electron beams are accelerated by voltages applied at gaps at discrete locations along the accelerator. At high currents, the beam itself induces wakefields in the accelerating gaps which can then feedback and distort the beam. The coupling of the gap-cavity modes and the beam can be characterized by frequency-dependent quantities known as the parallel and perpendicular gap impedances. Assessing the effects of instabilities resulting from these interactions requires accurate knowledge of these quantities. In this paper, we describe how a 3D finite-difference time-domain particle-in-cell code can be used to calculate both parallel and perpendicular gap impedances. We also demonstrate good agreement between full particle-in-cell simulations and results from a beam transport code making use of gap impedances to model beam centroid deflections. In practice, ferrite materials are often used in accelerating gaps to dampen cavity modes and reduce the severity of the resulting instabilities. We describe an implicit recursive convolution algorithm used to model the linear response of dispersive ferrite materials.

DOI: 10.1103/PhysRevAccelBeams.26.014602

I. INTRODUCTION

Linear induction accelerators (LIAs) have been used extensively to generate high-current electron beams for a wide variety of applications [1]. Each such accelerator is composed of a cylindrical vacuum beam pipe interrupted periodically by a sequence of accelerating gaps arranged at discrete locations along the beam pipe. We consider here the "core" variant of an LIA in which voltages at the gaps in the beam pipe are generated by inductive electric fields due to magnetic field swings in the ferromagnetic cores of the accelerating cell. This is in contrast to "driving circuit" LIAs, in which magnetic materials are eliminated by using low-impedance radial transmission lines to drive the cell [2]. Solenoids for focusing and dipole steering magnets, located between the gaps, are used to control the beam envelope and centroid position along the accelerator. The fundamental accelerating mechanism in a LIA is, of course, due to the voltages applied to the accelerating gaps which are distributed along the beam line. A charged particle beam propagating past a gap gains kinetic energy due to the gap voltage. To the lowest order, the voltage across the gap is given by the waveform generated by the pulsed power driver when applied to the full cell. However, at high currents, the beam itself induces wakefields in the accelerating gaps proportional to the current which alters the field structure, and hence the total voltage is seen by the beam.

For example, an on-axis axisymmetric beam induces axisymmetric ($m = 0$, where m is the azimuthal mode number) gap voltage variations which result in energy spread along the beam pulse, as upstream beam segments are affected by the wakefields induced by downstream segments. Even more importantly, an off-axis beam can generate $m = 1$ modes in the gap, which result in beam deflections. The coherent deflections of the beam as it passes through multiple accelerating gaps are known as beam-breakup instability (BBU) and can be especially problematic in electron LIAs [1,3–5]. The $m = 0$ energy spread instability is less important as it does not grow coherently along the beamline but may still have a deleterious effect on beam quality [6].

The strength of the $m = 0$ and $m = 1$ modes of excitation in a given gap can be characterized by parallel and perpendicular (or transverse) impedances, respectively.

*carstent@vosssci.com

To assess the expected severity of energy spread and BBU instabilities, it is important to be able to calculate the parallel and perpendicular impedances of the accelerating gaps [6]. For example, from analytic theory [1,4,5,7], the maximum centroid excursion magnitude, $\xi(z)$, after propagation through $N \gg 1$ periodic accelerating gaps, asymptotes as

$$\xi(z) = \xi_0[\gamma_0/\gamma(z)]^{1/2} \exp[\Gamma], \tag{1}$$

where the growth rate is given by

$$\Gamma(z) = \frac{1}{c} I_b N \mathrm{Re}(Z_\perp)\left\langle \frac{1}{B} \right\rangle, \tag{2}$$

where c is the speed of light, I_b is the beam current, γ is the Lorentz factor of the beam, $Z_\perp$ is the frequency-dependent complex transverse impedance of the gap (in units of Ohms per unit length), and $\langle 1/B \rangle$ is the average of the inverse of the focusing magnetic field. This asymptotic scaling has been verified in experiments on the DARHT–II accelerator at Los Alamos National Laboratory (LANL) [8], using measured values of $Z_\perp$ [9].

In principle, it is possible to use a particle-in-cell (PIC) code to model a full LIA in which the full geometry of both the gaps and the accelerating cells is included so that the effects of beam-induced wakefields are included self-consistently. But lengthy runtimes and numerical instabilities which emerge in large PIC simulations make this impractical for LIAs with many hundreds of accelerating cells.

A common method for modeling of lengthy LIAs is to make use of a beam transport code such as LAMDA [10,11]. In such a reduced model, the beam is assumed to be a circular rigid rotor, with the beam pulse decomposed into independent disks. Each discrete disk is characterized by its current, energy, radius, and centroid position. Envelope and centroid equations are solved for each disk as it propagates through the LIA, and the energy of the disk is incremented as it crosses an accelerating gap.

In the BBU model implemented in LAMDA, discrete transverse impulses are received by the centroid of each disk at a gap location. These impulses, due to beam-induced wakefields, can also be directly related to $Z_\perp$. In both the asymptotic estimation of Eq. (2) and in a beam-transport code such as LAMDA, the effect of BBU for specific gap and cell designs in an LIA requires knowledge of frequency-dependent $Z_\perp$.

A theoretical treatment for a simple pillbox geometry was performed by Briggs *et al.* [6] in which approximate expressions for parallel and perpendicular impedances are obtained. The resulting values of $Z_\parallel(\omega)$ and $Z_\perp(\omega)$ are found to have resonances near the TM_{0n0} and TM_{1n0} resonance frequencies of the cavity. The Q values (the ratio of the center frequency to the width of the peak) for these resonances depend sensitively on the impedance boundary condition at the maximum pillbox radius. From Eq. (2), it is clear that in order to minimize the effect of BBU, it is desirable to keep $Z_\perp(\omega)$ as small as possible. One means of accomplishing this is to dampen the resonances by adding a ferrite material into the accelerating cell [12].

Since only the simplest structures, such as the pillbox of Briggs *et al.* [6], allow for the analytic calculation of $Z_\parallel(\omega)$ and $Z_\perp(\omega)$, it is generally necessary to calculate these quantities numerically. One common tool used to numerically calculate $Z_\perp(\omega)$ is the code AMOS developed by DeFord, Craig, and McLeod [13]. This is a specialized finite-difference time-domain (FDTD) code in which the cell geometry is modeled using a 2D rz grid. Postprocessing of the FDTD results yields the frequency-dependent impedances. Since $Z_\perp$ is the response function due to an off-axis beam, the fields will be 3D in general. Azimuthal variation of the fields is modeled by decomposing the general 3D fields into azimuthal modes of a chosen order. The code has also been modified to model the frequency-dependent (linear, isotropic) permeability of ferrite materials used to dampen the response [12].

In this paper, we describe how $Z_\parallel$ and $Z_\perp$ can be calculated for an arbitrary 3D accelerating cell by a 3D PIC code including the effects of dispersive materials such as ferrites. For the PIC results presented in this paper, the CHICAGO [14,15] code is used, although the algorithms and methods described here could be easily implemented into any PIC code. CHICAGO is an advanced three-dimensional fully electromagnetic PIC code designed for executing multiscale plasma and beam physics simulations. As mentioned above, the numerical grid in AMOS is in 2D cylindrical rz coordinates and thus is restricted to axisymmetric cell geometries. By performing CHICAGO simulations in full 3D, this restriction is lifted.

To calculate $Z_\parallel$ and $Z_\perp$, it is sufficient to run CHICAGO with a rigid particle beam, in which the wakefields generated in the gaps are not allowed to feed back on the beam. It is also possible to perform fully self-consistent PIC simulations in which the beam is allowed to deflect naturally due to its own wakefields. The resulting centroid motion can then be compared to the beam-transport/BBU model.

The organization of the paper is as follows: In Sec. II, we review the theoretical results of Briggs *et al.* for a pillbox geometry and then demonstrate in Sec. III how both parallel and perpendicular impedances can be calculated by a 3D PIC simulation. In Sec. IV, we compare a fully self-consistent Chicago simulation of a short accelerator section with a single pillbox gap and compare the centroid behavior with results from LAMDA in which the gap is characterized by $Z_\perp$ for the gap. Good agreement between the two approaches is found. In Sec. V we discuss the modeling of ferrite materials as linear isotropic dispersive materials

using an implicit version of the recursive convolution algorithm for FDTD codes [16–18]. In Sec. VI, the method is verified by comparing the reflection and transmission coefficients of a TEM wave from a dispersive ferrite slab with analytic results. In Sec. VII, ferrite structures, used to damp cavity resonances, are introduced into the PIC simulation model. We then compare results from CHICAGO to published results from the AMOS code for a test gap geometry used on the ETA-II accelerator in Sec. VIII. In Sec. IX, we show a comparison of simulation and measurement results for the prototype accelerator cell (PAC) fielded at LANL [19]. This test cell has been used to assess the impedance of a block of gaps proposed for use in the Scorpius accelerator to be built at the Nevada test site [20]. Good agreement between simulation and measurement is found. Some conclusions and suggestions for future work follow in Sec. X.

II. CALCULATION OF PARALLEL AND PERPENDICULAR IMPEDANCES OF AN IDEALIZED ACCELERATING GAP

An idealized pillbox gap geometry for a LIA accelerating cell, as shown in Fig. 1, was assumed by Briggs *et al.* [6]. We here briefly review the main results of that work. When the gap is driven by a sinusoidal beam current, $I_b(\omega)$, along the radial axis, cavity modes are generated in the pillbox cylindrical cavity which can then feed back on the beam.

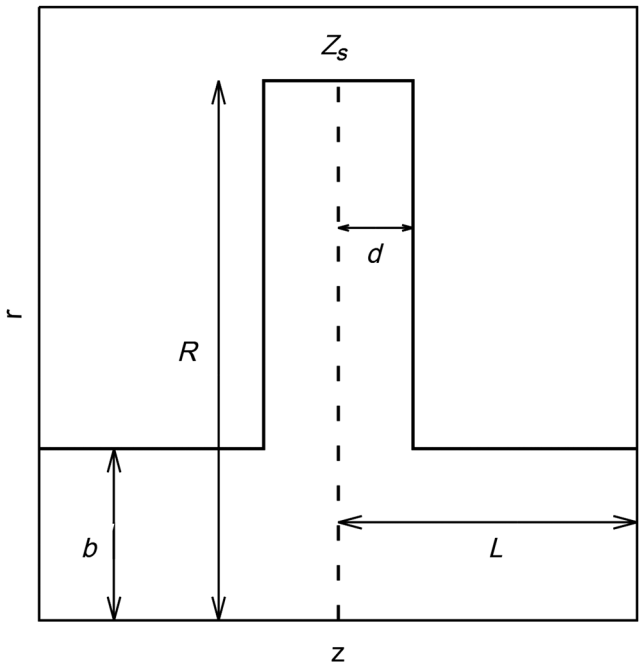

FIG. 1. Idealized geometry of LIA accelerating gap. The radial coaxial line is terminated at $r = R$ by an impedance of Z_S. The gap and beam pipe are both axisymmetric and bilaterally symmetric about the dashed vertical line. In the treatment of Briggs, $L \to \infty$.

For an on-axis and axisymmetric beam, TM_{0n0} cavity modes are generated in the gap which produce an induced voltage defined as

$$V(\omega) = -Z_{\parallel}(\omega) I_b(\omega), \tag{3}$$

where $Z_{\parallel}$, in units of Ohms, is known as the parallel impedance of the gap. The time-domain induced voltage is given immediately by the convolution theorem. This induced voltage can then feed back on the beam producing energy variations along the beam pulse. An off-axis beam can generate TM_{1n0} cavity modes which are the source of the BBU instability. These modes generate a transverse deflecting force upon beam particles traveling through the gap. If the beam is characterized in the time domain by a current, $I_b(t)$, and a beam offset in the x direction characterized by $\xi(t)$, the frequency-domain deflection impulse can be written as

$$\Delta p_x(\omega) = -\frac{i}{c} e Z_{\perp}(\omega) F(\omega), \tag{4}$$

where $Z_{\perp}(\omega)$, in units of Ohms/length, is known as the transverse impedance of the gap, and $F(\omega)$ is the Fourier transform of the product $I_b(t)\xi(t)$. For the simple pillbox geometry shown in Fig. 1, Briggs *et al.* find the following approximate formulas for $Z_{\parallel}(\omega)$ and $Z_{\perp}(\omega)$.

The parallel impedance of the pillbox gap is given by

$$Z_{\parallel}(\omega) = i \frac{4d}{bc} P(\omega), \tag{5}$$

where

$$P(\omega) = \frac{\sin^2(\omega d/c)}{(\omega d/c)^2} \frac{1}{H_0}, \tag{6}$$

$$H_0 = \frac{J_0'(\omega b/c)}{J_0(\omega b/c)} - \frac{G'(\omega b/c)}{G(\omega b/c)} + \frac{\omega}{cbd} \sum_n \frac{1 - e^{-2\nu_n d}}{\nu_n^3}, \tag{7}$$

$$G(\omega r/c) = J_0(\omega r/c) + C_0 N_0(\omega r/c), \tag{8}$$

$$C_0 = \frac{i(Z_s/Z_o) J_0'(\omega R/c) - J_0(\omega R/c)}{N_0(\omega R/c) - i(Z_s/Z_o) N_0'(\omega R/c)}, \tag{9}$$

$$\nu_n^2 = \beta_{0n}^2 - (\omega/c)^2, \tag{10}$$

and $J_m(z)$ and $N_m(z)$ are the mth order Bessel functions of the first and second kind, respectively, $\beta_{mn} b = x_{mn}$, where x_{mn} is the nth zero of $J_m(x)$, Z_s is the surface resistance used to terminate the gap, and

$$Z_o = 60\Omega \times (2d)/R \tag{11}$$

is the radial transmission line impedance at $r = R$. The analytic treatment used by Briggs assumes an infinitely

long beam pipe on either side of the gap, i.e., $L \to \infty$. Moreover, it is valid only for purely imaginary values of ν_n, i.e., that is $\omega \leq c\beta_{0n}$ for all nonzero positive integral values of n. Physically, above this frequency, for $n = 1$, the TM_{01} mode may propagate in the beam pipe, which has the lowest $m = 0$ cutoff frequency.

The transverse or perpendicular impedance of the pillbox gap is given by

$$Z_\perp(\omega) = i\frac{2d}{\pi\varepsilon c b^2} P_1(\omega), \tag{12}$$

where

$$P_1(\omega) = \frac{\sin^2(\omega d/c)}{(\omega d/c)^2}\frac{1}{H_1}, \tag{13}$$

$$H_1 = \left(\frac{\omega b}{c}\right)\left[\frac{J_1'(\omega b/c)}{J_1(\omega b/c)} - \frac{G_1'(\omega b/c)}{G_1(\omega b/c)}\right] - \frac{1}{d}\sum_n \frac{1-e^{-2\mu_n d}}{\mu_n(\rho_{1n}^2 b^2 - 1)} + \left(\frac{\omega}{c}\right)^2 \frac{1}{d}\sum_n \frac{1-e^{-2\varepsilon_n d}}{\varepsilon_n^3}, \tag{14}$$

$$G_1(\omega r/c) = J_1(\omega r/c) + C_1 N_1(\omega r/c), \tag{15}$$

$$C_1 = \frac{i(Z_s/Z_o)J_1'(\omega R/c) - J_1(\omega R/c)}{N_1(\omega R/c) - i(Z_s/Z_o)N_1'(\omega R/c)}, \tag{16}$$

$$\varepsilon_n^2 = \beta_{1n}^2 - (\omega/c)^2, \tag{17}$$

$$\mu_n^2 = \rho_{1n}^2 - (\omega/c)^2, \tag{18}$$

and $\rho_{mn} b = x'_{mn}$, where x'_{mn} is the mth zero of $J'_m(x)$. The above treatment is valid for $\omega \leq c\beta_{1n}$ for all nonzero positive integral values of n. Physically, above the threshold frequency, for $n = 1$, the TE_{11} mode may propagate in the beam pipe.

III. $Z_\parallel$ AND $Z_\perp$ CALCULATIONS WITH CHICAGO OF IDEALIZED GAP

Parallel and perpendicular impedances are usually calculated by specialized stand-alone codes such as AMOS [21]. We here verify the use of CHICAGO to calculate these quantities and compare our time-domain PIC results with the Briggs results for a simple axisymmetric pillbox gap. The parallel impedance of the gap can be calculated in 2D rz cylindrical coordinates. The simulation geometry is shown in Fig. 1 with exact dimensions given by $b = 7.5$ cm, $d = 3.5$ cm, $R = 30$ cm. The surface resistivity, Z_s, is applied to the boundary at $r = R$, from $z = -d$ to d. An arbitrary dimensionless surface impedance ratio, Z_s/Z_o, can be chosen, where $Z_o = 10\Omega$ [Eq. (11)]. In the treatment of Briggs, the beam pipe is infinitely long. In the simulation, a finite length of L must be chosen. One-way wave equations [16] are applied at the boundaries from $r = 0$ to b, at $z = -L$ and L, where $L = 60$ cm. Note that such boundary conditions guarantee the perfect transmission of outgoing TEM modes in the pipe at the boundary planes but may reflect outgoing TE and TM modes. A particle beam is injected into the simulation space at the left-hand boundary with a Gaussian pulse shape given by

$$I_b(t) = I_o e^{-(t-t_o)^2/\tau^2}, \tag{19}$$

with $\tau = 0.3$ ns. We note here that the simulation is driven with a stiff beam, i.e., composed of very massive particles ($\gg m_e$). This is because we are seeking to characterize only the properties of the gap when driven by a current, encapsulated in the response function, $Z_\parallel$. The feedback of the wakefields generated by the gap on the beam particles is neglected here by using an effectively infinite particle inertia. The voltage across the gap at $r = b$, $V(t)$, can be tabulated as a function of time during the simulation. Then, from Eq. (3), the ratio of the (discrete) Fourier transforms of $V(t)$ and $-I_b(t)$ yields $Z_\parallel$. Note that the time shift t_o in Eq. (19) is chosen so that $I_b(t)$ corresponds to the current seen at the gap center, $z = 0$.

The perpendicular impedance can be calculated by a similar procedure. Following Briggs, the deflection impulse on a test particle passing through an accelerating gap region is given by integration of the Lorentz force, where the integration is performed along the particle trajectory, given by $z = v(t - t_o)$ where $v \simeq c$ for a relativistic particle. This yields the expression

$$\Delta p_x = \frac{e}{c}\int_{-\infty}^{\infty}(E_x - cB_y)dz. \tag{20}$$

Briggs calculates this integral for an arbitrary test-particle transverse position in the beam pipe ($r \leq b$). The result is found to be independent of r and azimuthal angle, θ, with the resulting impulse (in the frequency domain) given by Eq. (12).

In a 3D cylindrical PIC simulation, we can calculate the time-domain impulse response by performing the integration of Eq. (20) at a radial position of $r = b$ and angle of $\theta = \pi/2$. At this angle, $E_x = -E_\theta$ and $E_\theta(b)$ is zero on the conductor walls. Likewise, $B_y = B_r$ and $B_r(b)$ is zero on the conductor walls. The time-domain impulse can then be written as

$$\Delta p_x = -\frac{e}{c}\int_{-d}^{d}[E_\theta(b, \pi/2, z) + cB_r(b, \pi/2, z]dz, \tag{21}$$

which is a simple line integral that can be calculated at arbitrary time intervals in a PIC simulation. If the simulation is run with an injected beam with a known current pulse and offset, $Z_\perp$ can be calculated from the Fourier

transform of the impulse, $\Delta p_x(\omega)$, and the current-offset product, $I_b(t)\xi(t)$, from Eq. (4). Note again that the time-domain beam current and offset values are evaluated at the gap center $z = 0$.

An axisymmetric beam is used to calculate the parallel impedance, and the pillbox geometry of the simplified gap model is axisymmetric as well, so the $Z_\parallel$ simulation can be done in 2D-rz coordinates. Of course, in general, a full 3D simulation is necessary if there is an azimuthal structure in the beam pipe or gap. In the case of an offset beam, full 3D is required even if the beam pipe and gap geometry are axisymmetric. The 2D simulation is performed with uniform cells with $\Delta r = \Delta z = 0.25$ cm. The 3D simulations are also performed in cylindrical coordinates with $\Delta\theta = \pi/10$. We note that it is also possible to calculate both $Z_\parallel$ and $Z_\perp$ from a single 3D simulation, as there is very little azimuthal variation in the pillbox gap voltage for a small beam offset. The injected current has a Gaussian pulse shape, as in Eq. (19), with $\tau = 0.3$ ns. This value of τ provides significant bandwidth to give good results out to several GHz. At higher frequencies, the signal-to-noise ratio degrades in the deconvolution of Eqs. (3) and (4). In the 3D simulation, the beam is offset by 0.25 cm in the $+x$ direction. Good results are found for offsets on the order of a single transverse cell width, Δr. The field solution in the simulations is performed by an implicit algorithm in which both electric and magnetic fields are advanced at full integral time step values. This algorithm is discussed in more detail in Sec. V C.

The results comparing the CHICAGO simulations with the Briggs model are shown in Fig. 2 for values of Z_s/Z_o given by 1/4 (black traces), 1 (red), and 4 (blue). There is seen to be good agreement between the simulated (solid lines) and theoretical (dotted) results for the real parts of $Z_\parallel$ and $Z_\perp$ (the imaginary parts are not plotted but the agreement is comparable to that of the real parts).

We note again that the Briggs treatment for an idealized pillbox geometry is characterized by the adjustable dimensionless parameter, Z_s/Z_o, which represents the relative termination impedance of the cavity. For $Z_s/Z_o \ll 1$, the outer radius of the cavity is effectively shorted, while, for $Z_s/Z_o \gg 1$, the outer radius of the cavity is effectively an open circuit. In these two limiting cases, the fields of the pure pillbox (i.e., in the absence of the beam pipe) cavity modes are known in closed form. For $Z_s/Z_o \to 0$, the radial dependence of the longitudinal field component (E_z) of the TM_{mn0} modes is given by $J_m(x_{mn}r/R)$, and the resonant frequencies are given by $\omega = cx_{mn}/R$. In the opposite limit, $Z_s/Z_o \to \infty$, the radial dependence of E_z is given by $J_m(x'_{mn}r/R)$, and the resonant frequencies of the cavity modes are given by $\omega = cx'_{mn}/R$.

In Fig. 2, the results for $Z_s/Z_o = 1/4$ are shown as black traces. In this case, we expect the cavity modes to be similar to the short-circuit case. For $Z_\parallel$, the peaks are indeed close to the short-circuit resonance frequencies for TM_{010} ($f = 380$ MHz), TM_{020} (880 MHz), and TM_{030} (1380 MHz). Higher order modes ($n > 3$) lie above the beam pipe TM_{01} cutoff frequency of 1530 MHz. For $Z_\perp$, the peaks are near the resonance frequencies for the short-circuit cavity modes: TM_{110} (610 MHz), TM_{120} (1120 MHz), with higher order modes again above the beam pipe cutoff frequency. For $Z_s/Z_o = 4$ (blue traces in Fig. 2), the cavity modes should be similar to the open circuit case. For $Z_\parallel$, the peaks are indeed close to the open-circuit resonance frequencies for TM_{010} (610 MHz) and TM_{020} (1120 MHz), and for $Z_\perp$, the peaks are near the open-circuit resonance frequencies for TM_{110} (290 MHz) and TM_{120} (850 MHz). All higher order modes again lie above the appropriate beam pipe cutoff frequency. Finally, for $Z_s/Z_o = 1$ (red traces in Fig. 2), the peaks of the resonances lie somewhere between the other two cases and are strongly damped by losses due to surface resistance. Note that in all cases, the Qs of the peaks are on the order of $\max(Z_s/Z_o, Z_o/Z_s)$.

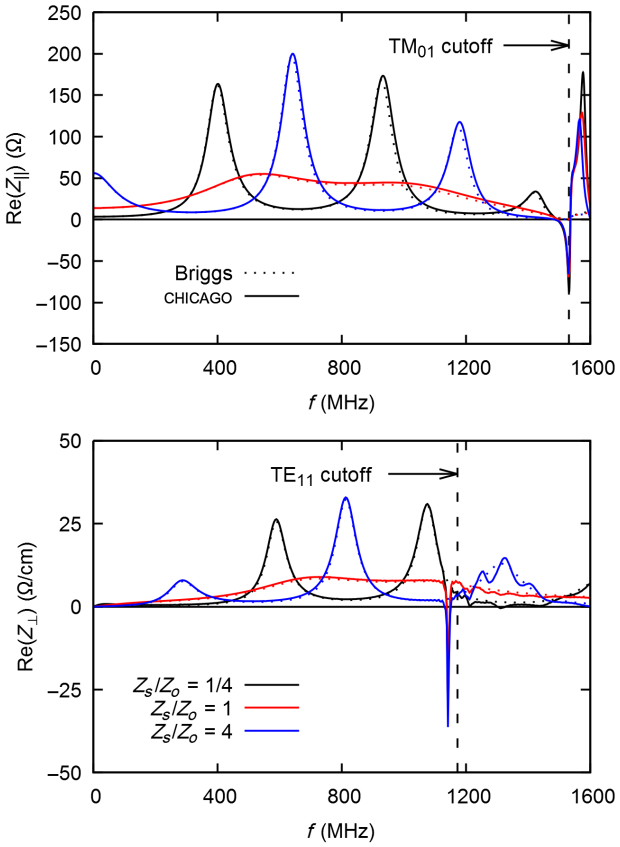

FIG. 2. $Z_\parallel$ (top) and $Z_\perp$ (bottom) for idealized pillbox gap with $b = 7.5$ cm, $d = 3.5$ cm, $R = 30$ cm, with terminating surface resistances of $Z_s/Z_o = 1/4$ (black), 1 (red), and 4 (blue). Results are shown for the theory of Briggs (dotted lines) and CHICAGO simulations (solid lines). For the CHICAGO results, $L = 60$ cm.

In both plots in Fig. 2, the results are plotted out to a value above the maximum frequency values, as discussed above, allowed by the Briggs treatment, 1530 MHz for $Z_\parallel$,

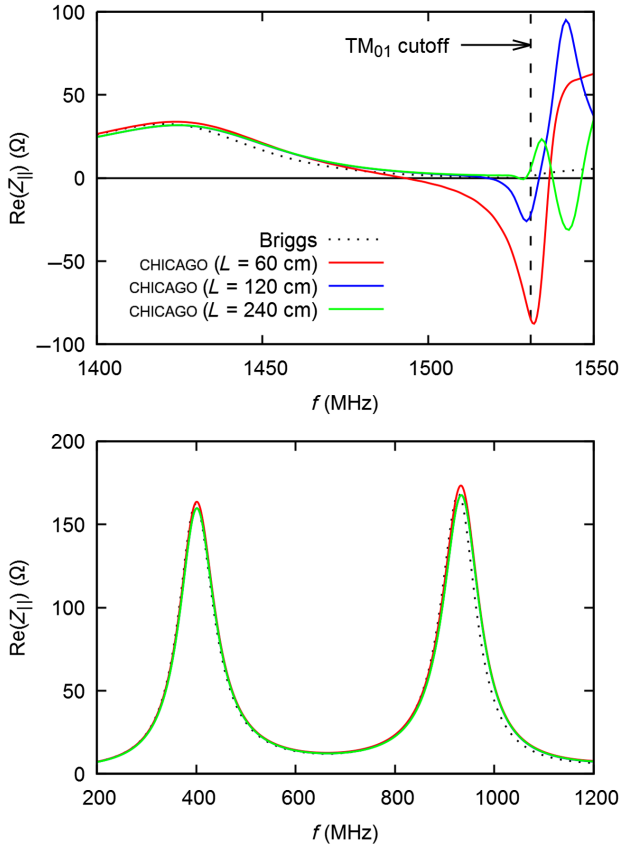

FIG. 3. $Z_\parallel$ plotted as a function of frequency for an idealized pillbox gap with $b = 7.5$ cm, $d = 3.5$ cm, $R = 30$ cm, and $Z_s/Z_o = 1/4$. Results are shown for the theory of Briggs (dotted line) and CHICAGO simulations (solid lines) with $L = 60$ cm (red), 120 cm (blue), and 240 cm (green). Top: detail in the region close to TM_{01} cutoff frequency. Bottom: effect of varying L at a lower frequency.

and 1160 MHz for $Z_\perp$, which correspond to the lowest $m = 0$ and $m = 1$ cutoff frequencies of the beam pipe. The PIC results are also suspect above these cutoff frequencies as well, due to the use of one-way wave equations at the longitudinal boundaries, as outgoing propagating TE and TM modes are not properly handled by such simple boundary conditions. Below the exact cutoff frequency, spatial profiles of evanescent modes can also extend to the simulation boundaries at $z = \pm L$, where $L = 60$ cm in this case. This can lead to unphysical reflections of TE and TM pipe modes even below the cutoff.

This effect can be seen explicitly in Fig. 2 in the CHICAGO results for both $\mathrm{Re}(Z_\parallel)$ and $\mathrm{Re}(Z_\perp)$, where there is a zero crossing and a local minimum slightly below the TM_{01} and TE_{11} cutoffs, respectively. This can be largely remedied by extending the longitudinal length of the simulation. This can be seen in the top plot of Fig. 3 in which $\mathrm{Re}(Z_\parallel)$ is plotted for the case $Z_s/Z_o = 1/4$ near the TM_{01} cutoff frequency. The Briggs result is shown again as a (black) dotted line and the CHICAGO results are shown as solids lines. Results from CHICAGO simulations with $L = 60$ cm (red), 90 cm (blue), and 120 cm (green) are shown in the plot. The Briggs result never becomes negative and exhibits only a kink discontinuity at the cutoff frequency. The CHICAGO results are seen to approach the theoretical ($L \to \infty$) results as L is increased. The problem of artificial boundary reflections of both evanescent and propagating pipe modes could, in principle, be largely circumvented with a more careful treatment of the longitudinal boundaries. This could be done by utilizing, for example, perfectly matched absorption layers [22–24], but this is beyond the scope of the present paper. The effect of varying L at frequencies well below the cutoff is shown in the bottom plot of Fig. 3. The peak values of $\mathrm{Re}(Z_\parallel)$ at the resonant frequencies are seen to converge rapidly for $L/b > 10$. The results are also found to be well converged with grid resolution and time step. The remaining slight discrepancy with the Briggs result can perhaps be partially attributed to small approximations made in the theory [6] regarding the treatment of the boundary at $r = b$.

IV. SELF-CONSISTENT BEAM DEFLECTION IN PILLBOX GAP

In the previous section, the CHICAGO simulations used to calculate $Z_\perp$ for a pillbox gap were performed with a rigid offset beam in which the wakefields induced in the gap were not allowed to feed back on the beam. In this section, we relax this constraint and perform a full PIC simulation in which the offset beam is self-consistently deflected by the gap. The results of this simulation can then be directly compared to the BBU model used in the beam transport code LAMDA [10,11] in which discrete transverse impulses are applied at gaps that are characterized by a frequency-dependent $Z_\perp$. This is a standard reduced model by which BBU effects are modeled for LIA designs [11,19].

In LAMDA a finite beam pulse is characterized by a current, $I_b(t)$, in which t is defined as the time measured back from the beam head, which is at $t = 0$, by definition. In the numerical implementation, the pulse is subdivided into a sequence of temporal disks of width Δt, each denoted by its discrete time. For each disk, envelope and centroid equations [10] are advanced in z, along the accelerator axis. Both $m = 0$ voltage perturbations and $m = 1$ centroid deflections at gap locations can be applied to disks by incorporating $Z_\parallel(f)$ and $Z_\perp(f)$ gap data (see Eqs. (3) and (4), respectively). In the following, we consider only gap deflections, as this is the root cause of BBU. But voltage perturbations can be treated in an analogous manner. The LAMDA code uses a narrow-gap approximation so that the full transverse impulse is applied to each disk at the center of the gap. The impulse of a disk at time t is given by the inverse Fourier transform of Eq. (4) for a centroid displacement in the x direction, with an analogous equation for a y displacement. Making use of the convolution theorem, we obtain

$$\Delta p_x(t) = \int_{-\infty}^{\infty} \Delta p_x(f) e^{-i2\pi f t} df = -\frac{ie}{c} \int_0^t Z_\perp(t-t') I_b(t') \xi(t') dt',$$
$$\Delta p_y(t) = \int_{-\infty}^{\infty} \Delta p_y(f) e^{-i2\pi f t} df = -\frac{ie}{c} \int_0^t Z_\perp(t-t') I_b(t') \eta(t') dt', \quad (22)$$

where $\xi(t)$ and $\eta(t)$ are the time-dependent centroid offsets in the x and y direction, respectively, and $Z_\perp(t)$ and $Z_\perp(f)$ are Fourier transform pairs. In Eq. (22), we have assumed an axisymmetric gap geometry. If this symmetry is broken, the gap must be characterized by two separate impedance functions $Z_{\perp x}$ and $Z_{\perp y}$ in both the frequency and time domains. This case is considered in greater detail in the following sections. Note that a real time-domain impulse requires $\mathrm{Re}[Z_\perp(f)]$ to be antisymmetric and $\mathrm{Im}[Z_\perp(f)]$ to be symmetric. For both the Briggs and CHICAGO results given in the previous section, this is true only when $|f|$ is less than the TE_{11} cutoff frequency. In LAMDA, a discretized version of the convolution theorem allows the time-domain impulses at gap locations to be calculated from the frequency-domain $Z_\perp$ and the Fourier transforms of the current-displacement products: $I_b(t)\xi(t)$ and $I_b(y)\eta(t)$. The envelope and centroid equations are used to advance the beam disks along the accelerator in z between gap locations.

We again consider an axisymmetric beam pipe and gap, as shown in Fig. 1, with $b = 7.5$ cm, $d = 2.5$ cm, $R = 27$ cm, and $Z_s/Z_o = 4$. Both the CHICAGO and LAMDA simulations are performed with $L = 60$ cm. In the CHICAGO simulation, a nondiverging 1-cm radius beam with a uniform density cross-section is injected at $z = -L$ as shown in the top of Fig. 4 and allowed to propagate through the simulation space. The current pulse at the injection plane, with rise and fall times on the order of 5 ns, is shown at the bottom of Fig. 4. The peak current is 2.92 kA, and the initial beam potential is 4 MV. There is a uniform applied magnetic field in the z direction of 1 kG. The emittance of the beam (~ 0.2 cm rad) is adjusted to maintain a matched beam, i.e., constant beam radius [25], for the length of the simulation. The CHICAGO simulation is performed in 3D cylindrical coordinates with $\Delta r = \Delta z = 0.25$ cm, 64 azimuthal spokes, and $c\Delta t = 0.1$ cm.

In the LAMDA simulation, the 60-ns pulse is modeled by 800 discrete disks, and the envelope and centroid equations are advanced by a spatial step size of 0.5 cm. Transverse centroid impulses are applied at the gap center, and the gap is modeled by the Briggs result for $Z_\perp(f)$, with a fitted correction that is matched to the theory at a frequency just below the beam cutoff. This is required to ensure a purely real temporal impulse, as discussed above.

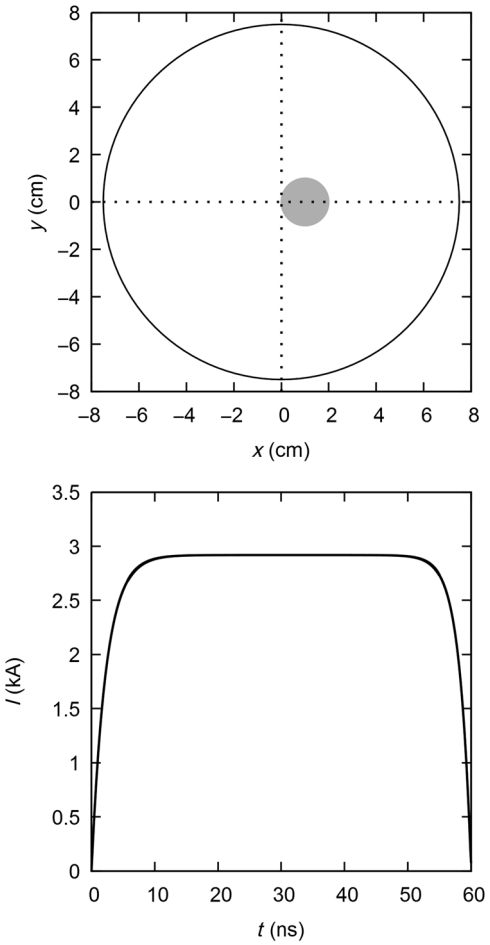

FIG. 4. Top: injected beam current density profile for 3D cylindrical CHICAGO beam deflection simulation. The beam is injected into the pipe ($b = 7.5$ cm) at $z = -60$ cm. An ideal pillbox gap is centered at $z = 0$ with $d = 2.5$ cm, $R = 27$ cm, and $Z_z/Z_o = 4$. Bottom: injected beam current as a function of time.

The results for the beam centroid displacement are shown as a function of z at a simulation time of $t = 30$ ns in Fig. 5. In this context, t is the actual CHICAGO simulation time and does not represent a beam-frame disk time. At this time, the entire simulation space is filled by the full-current flattop portion of the beam, with the 5-ns rising beam head having exited the simulation and the tail has not yet entered. For the CHICAGO simulation, the beam centroid position is calculated from the transverse mean values, $\langle x \rangle$ and $\langle y \rangle$, of the particle positions at fixed values of z along the grid. Good agreement is found between the CHICAGO and LAMDA results. In the CHICAGO simulation, there is no evidence of emittance growth or any other "nonideal" effects which are neglected in LAMDA. The gap center and width are shown in the figure (by a dashed line and gray rectangular area, respectively). The effect of the narrow gap approximation in LAMDA is clearly visible in the data for $\langle x \rangle$, where a sharp

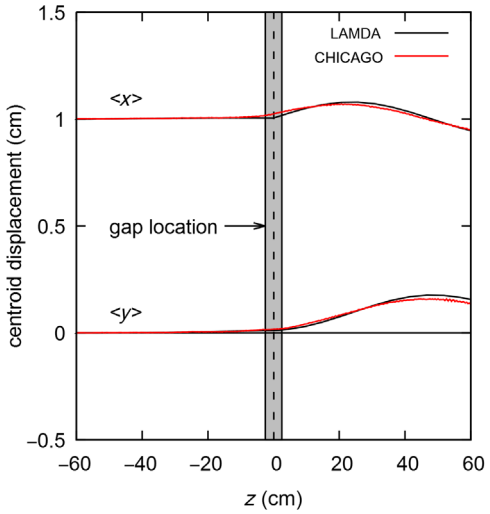

FIG. 5. Centroid displacement as a function of z at $t = 30$ cm for a beam deflected by a pill-box gap. Results from the beam transport code LAMDA are shown in black and CHICAGO 3D cylindrical simulation results are shown in red.

discontinuity in slope is seen at the gap center. The CHICAGO result exhibits a more gradual change in the slope of $\langle x \rangle$ in the region around the gap due to the effect of the finite gap width. We note also that by construction, $Z_\perp(f)$ includes only the effect of the perturbed fields in the $m = 1$ mode and is therefore limited to the regime where the displacement magnitude and beam radius are small compared to b. The CHICAGO results (modeled by many azimuthal spokes) also include corrections, presumably small, due to higher-order modes supported by the grid.

The general good agreement between the two approaches demonstrates that BBU growth can be well approximated by a simplified beam transport code such as LAMDA in which gaps are characterized by the perpendicular impedance. The LAMDA code has also previously been shown to give good agreement with experimental BBU measurements in the DARHT accelerators at LANL [11].

V. FERRITE MODELING BY RECURSIVE CONVOLUTION METHOD OF LINEAR DISPERSION

Ferrites are used in LIA gaps both to provide an inductive load to the pulse power cell and to dampen rf cavity modes which can lead to the beam-breakup (BBU) instability. To capture the damping effect of ferrites, it is sufficient to consider the linear response of the material [12]. To facilitate the modeling of ferrites in the LIA cell simulations, it was necessary to develop linear dispersion models for use in CHICAGO. A rudimentary version of such an algorithm for magnetic dispersion (i.e., frequency-dependent permeability) was previously included in Chicago but was limited to explicit EM field solvers. We have extended the algorithm to allow it to work with implicit field solvers and to allow for electric dispersion as well (frequency-dependent permittivity). In this section, we describe our implementation of a recursive convolution algorithm for linear dispersion [17,18]. The treatment is similar to the description given by Taflove [16] for use with explicit field solvers.

A. Electric dispersion

In a linear homogeneous isotropic dispersive media, the frequency-domain constitutive relation between electric displacement and field can be written as

$$\vec{D}(\omega) = \varepsilon(\omega)\vec{E}(\omega), \tag{23}$$

where

$$\varepsilon(\omega) = \varepsilon_\infty + \chi_E(\omega) \tag{24}$$

and $\chi_E(\omega)$ is the Fourier transform of the time-domain susceptibility, $\chi_E(t)$. For a given material, ε is generally given as a function of ω. By the convolution theorem, the time-domain displacement is given by

$$\vec{D}(t) = \varepsilon_\infty \vec{E}(t) + \chi_E(t) * \vec{E}(t), \tag{25}$$

where the "$*$" operator represents the convolution integral.

The recursive convolution algorithm is obtained by assuming a time-domain susceptibility of the form

$$\begin{aligned}\chi_E(t) &= \sum_{i=1}^{N} [A_i \sin(\omega_i t) + B_i \cos(\omega_i t)] e^{-\alpha_i t}\theta(t) \\ &= \sum_{i=1}^{N} \mathrm{Im}(G_i e^{-\gamma_i t})\theta(t),\end{aligned} \tag{26}$$

where

$$G_i = A_i + iB_i, \tag{27}$$

and

$$\gamma_i = \alpha_i - i\omega_i, \tag{28}$$

and $\theta(t)$ is the Heaviside step function. The value of ε_∞ and the set of coefficients, A_i, B_i, α_i, and ω_i for $i = 1, 2, \ldots N$ are chosen by fitting the Fourier transform of $\chi_E(t)$ to available permittivity data, $\varepsilon(\omega)$. With this ansatz, the time-domain constitutive relation can be written as

$$\vec{D}(t) = \varepsilon_\infty \vec{E}(t) + \sum_{i=1}^{N} \mathrm{Im}(\vec{\psi}_{Ei}(t)), \tag{29}$$

where

$$\vec{\psi}_{Ei}(t) = (G_i e^{-\gamma_i t}) * \vec{E}(t) = G_i \int_{-\infty}^{t} e^{-\gamma_i (t-t')} \vec{E}(t') dt'. \quad (30)$$

A (second-order accurate) numerical approximation for the convolution integral, assuming a uniform time step, Δt, is given by

$$\vec{\psi}_{Ei}^{n} \simeq G_i \Delta t \left[\sum_{m=0}^{n-1} e^{-\gamma_i \Delta t (n-m)} \vec{E}^m + \vec{E}^n/2 \right], \quad (31)$$

where the superscript index denotes the time level of the quantity. Explicitly,

$$\vec{E}^n = \vec{E}(t = n\Delta t), \quad (32)$$

etc. We have also assumed that $\vec{E}^0 = 0$, that is, there are no initial fields in the dielectric. Defining the discretized polarization vector,

$$\vec{P}_i^n = (\vec{\psi}_{Ei}^n - G_i \Delta t \vec{E}^n/2)/\Delta t = G_i \sum_{m=0}^{n-1} e^{-\gamma_i \Delta t (n-m)} \vec{E}^m, \quad (33)$$

we can easily show that

$$\vec{P}_i^0 = \vec{0}, \quad (34)$$

and

$$\vec{P}_i^n = e^{-\gamma_i \Delta t} [\vec{P}_i^{n-1} + G_i \vec{E}^{n-1}] \quad (35)$$

for $n \geq 1$. The discretized time-domain constitutive relation can then be rewritten as

$$\vec{D}^n = \tilde{\varepsilon} \vec{E}^n + \Delta t \sum_{i=1}^{N} \mathrm{Im}(\tilde{P}_i^n), \quad (36)$$

where

$$\tilde{\varepsilon} = \varepsilon_\infty + \frac{\Delta t}{2} \sum_{i=1}^{N} B_i. \quad (37)$$

The recursion relation for the sum of the polarization vectors can then be used to update the electric displacement, by using only the present and previous time step electric field value, rather than by calculating the full numerical convolution including all old electric field values.

B. Magnetic dispersion

The treatment for magnetic dispersion follows a nearly identical treatment, with the time domain constitutive relation given by

$$\vec{B}(t) = \mu_\infty \vec{H}(t) + \chi_B(t) * \vec{H}(t), \quad (38)$$

The magnetic susceptibility is assumed to have the same form as the electric susceptibility:

$$\chi_B(t) = \sum_{i=1}^{N} (A_i \sin(\omega_i t) + B_i \cos(\omega_i t)) e^{-\alpha_i t} \theta(t), \quad (39)$$

in which μ_∞ and the coefficients in the sum, A_i, B_i, α_i, and ω_i, are chosen, in this case, by fitting the permeability data, $\mu(\omega)$. By the same procedure as above, the time-domain magnetic constitutive relation can be written

$$\vec{B}^n = \tilde{\mu} \vec{H}^n + \Delta t \sum_{i=1}^{N} \mathrm{Im}(M_i^n), \quad (40)$$

where

$$\tilde{\mu} = \mu_\infty + \frac{\Delta t}{2} \sum_{i=1}^{N} B_i, \quad (41)$$

with magnetization vectors given by the recursion relation

$$\vec{M}_i^n = e^{-\gamma_i \Delta t} [\vec{M}_i^{n-1} + G_i \vec{H}^{n-1}], \quad (42)$$

where G_i and γ_i are defined as above for the electric dispersion case.

C. Implicit field solve with time-domain constitutive relations

An implicit field solution is obtained by discretizing Maxwell's equations,

$$\frac{\partial \vec{B}}{\partial t} = -\nabla \times \vec{E}, \quad (43)$$

$$\frac{\partial \vec{D}}{\partial t} = -\nabla \times \vec{H} - \vec{J}, \quad (44)$$

and employing the discretized constitutive relations given by Eqs. (36) and (40). We then obtain the equations for the implicit field advance, with both $\vec{E}$ and $\vec{H}$ at full integral time levels,

$$\begin{aligned} &\tilde{\varepsilon} \vec{E}^{n+1} - (1+\alpha) \frac{\Delta t}{2} (\nabla \times \vec{H})^{n+1} \\ &\quad = \tilde{\varepsilon} \vec{E}^n + (1-\alpha) \frac{\Delta t}{2} (\nabla \times \vec{H})^n \\ &\qquad - \Delta t \sum_i \mathrm{Im}(\tilde{P}_i^{n+1} + \tilde{P}_i^n) - \Delta t \vec{J}^{n+1/2}, \end{aligned} \quad (45)$$

$$\begin{aligned} &\tilde{\mu} \vec{H}^{n+1} + (1+\alpha) \frac{\Delta t}{2} (\nabla \times \vec{E})^{n+1} \\ &\quad = \tilde{\mu} \vec{H}^n - (1-\alpha) \frac{\Delta t}{2} (\nabla \times \vec{E})^n - \Delta t \sum_i \mathrm{Im}(\tilde{M}_i^{n+1} + \tilde{M}_i^n). \end{aligned} \quad (46)$$

The dimensionless parameter, α, with a value between zero and unity is known as the time-biasing coefficient [26,27]. The default value of $\alpha = 0$ results in a time-centered second–order accurate field solve. But a small nonzero positive value can be useful at times to damp high–frequency noise in the simulation. All the CHICAGO simulations discussed in this paper were performed with $\alpha \sim 0.1$. The recursion relations, Eqs. (35) and (42), are used to advance $\vec{P}_i$ and $\vec{M}_i$, respectively.

D. Fitting of permeability data for the recursive convolution algorithm

In this section, we describe how arbitrary permittivity and permeability data may be fitted to the form given by Eq. (26), which allows for the use of recursive convolution algorithms. Following Taflove [16], we assume that an arbitrary susceptibility can be written as a weighted linear sum of simplified response functions in the form of Eq. (26), with weighting coefficients chosen to fit the desired data set. We first discuss the two simple susceptibility models and then demonstrate how these models may be used to fit measured permeability data for the ferrite material PE11BL [12].

1. Susceptibility models

To use the recursive convolution models described above, it is necessary to model (electric or magnetic) susceptibilities as a sum of terms which may be written in the time-domain as

$$\chi(t) = \mathrm{Im}(Ge^{-\gamma t})\theta(\mathrm{t}), \tag{47}$$

where G and γ are complex constants. We consider two possible (dimensionless) susceptibility models [16]. We first consider a Debye relaxation model which is defined in the frequency domain as

$$\chi_D(\omega) = \frac{2}{1 - i\omega\tau}, \tag{48}$$

where τ is a relaxation time. The function is normalized so that $\mathrm{Im}[\chi_D(\tau^{-1})] = 1$ as can be seen in the top plot of Fig. 6, which shows a plot of a sample Debye relaxation with $\tau = 1.6$ ns $(1/2\pi\tau = 100$ MHz) as a function of $f = \omega/2\pi$. From the inverse Fourier transform of $\chi_D(\omega)$, we find

$$G_D = 2\tau^{-1}, \tag{49}$$

$$\gamma_D = \tau^{-1}. \tag{50}$$

The second model is the Lorentzian response, defined as

$$\chi_L(\omega) = \left(\frac{2\delta}{\omega_o}\right)\frac{\omega_o^2}{\omega_o^2 - 2i\omega\delta - \omega^2}, \tag{51}$$

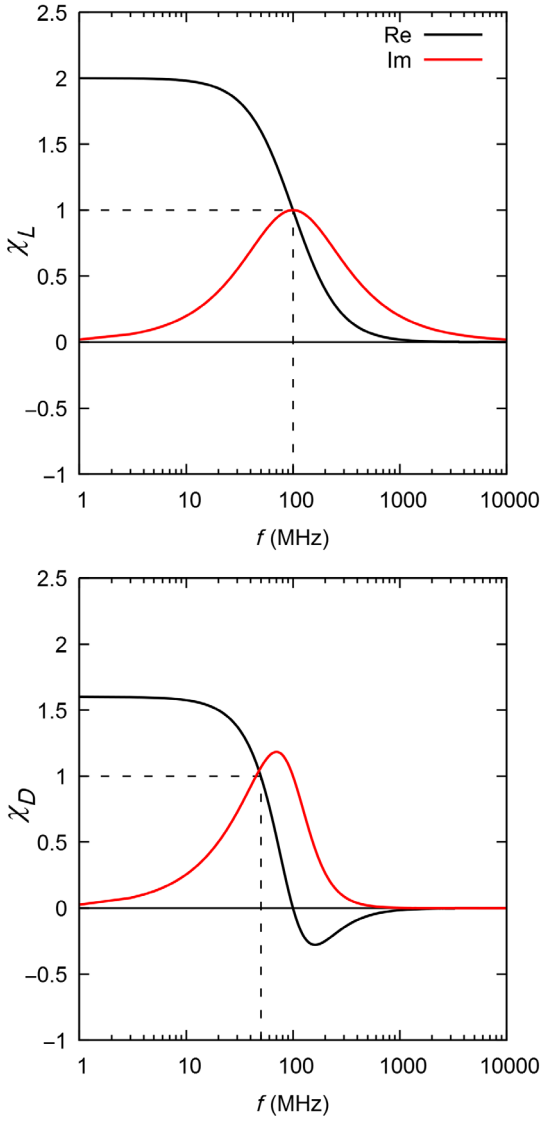

FIG. 6. Response function examples. Top: Debye relaxation $\tau = 1.6$ ns, Bottom: Lorentzian $f_o = 50$ MHz and $\delta = 250$ MHz.

where $\omega_o = 2\pi f_o$ is the (real) angular resonance frequency and δ is the (real) decay constant with units of inverse time. The function is normalized so that $\mathrm{Im}[\chi_\mathrm{L}(\omega_\mathrm{o})] = 1$, as can be seen in the bottom of Fig. 6 which shows a sample Lorentzian response with $f_o = 50$ MHz and $\delta = 250$ MHz. In this case, we find that

$$G_L = \frac{2i\delta}{\omega_o}\frac{\omega_o^2}{\sqrt{\omega_o^2 - \delta^2}}, \tag{52}$$

$$\gamma_L = \sqrt{\omega_o^2 - \delta^2} - i\delta. \tag{53}$$

Note that both χ_D and χ_L are proper linear response functions that satisfy Kronig-Kramers relations, ensuring proper causal behavior. For arbitrary permittivity or

permeability data, the frequency-dependent susceptibilities may be modeled as a linear combination of Lorentzian and/or Debye relaxation response functions,

$$\chi(\omega) = \sum_i C_i \chi_i(\omega), \tag{54}$$

where $\chi_i = \chi_D$ or χ_L, and C_i is a dimensionless fitting constant. This linear fit can be used to model any general rational function [16]. In practice, one can obtain an excellent fit to data by including a sufficient number of terms in the sum.

2. Fitting of permeability data for PE11BL ferrite

As an example, we consider the data and fit presented by DeFord [12] for the PE11BL ferrite, shown in Fig. 7. The experimental data shown in the figure are fitted to a sum of two Lorentzians with the following parameters: $C_1 = 7.90$, $f_{o1} = 0.67$ GHz, and $\delta_1 = 50$ GHz for the first Lorentzian, and $C_2 = 8.98$, $f_{o2} = 0.26$ GHz, and $\delta_2 = 50$ GHz for the second. The imaginary parts of the two separate Lorentzians functions are shown as red dashed lines. This two-term fit is seen to be in good agreement with experimental data in the frequency range from 1 MHz to 1 GHz. As mentioned above, the experimental data can be fitted more closely by including a larger number of Lorentzians (an example of a more careful fitting is given in Sec. IX below) but for the present, to illustrate the use of the ferrite model in the following sections, we retain the two-term fit used by DeFord.

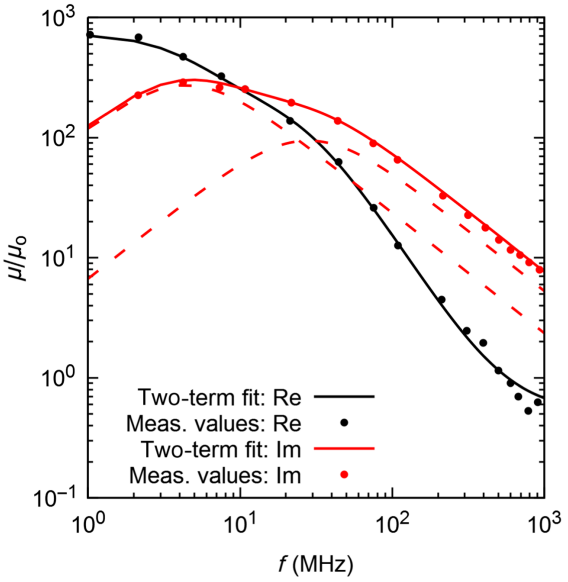

FIG. 7. Experimental data and two-term Lorentzian fit for permeability of PE11BL ferrite. The imaginary parts of the two separate Lorentzians are shown as red dashed lines. Parameters used for the fit are $C_1 = 7.90$, $f_{o1} = 0.67$ GHz, and $\delta_1 = 50$ GHz, $C_2 = 8.98$, $f_{o2} = 0.26$ GHz, and $\delta_2 = 50$ GHz for the second. Adapted from Ref. [12]

VI. 1D TEST OF FERRITE MODEL IN CHICAGO

To demonstrate the use of the linear dispersion model described above, we consider a 1D Cartesian test problem in which an incident TEM wave of a fixed frequency, ω, is incident on a slab of width d, characterized by $\varepsilon(\omega)$ and $\mu(\omega)$. By applying appropriate boundary matching conditions on the front and rear faces of the slab, the reflection (R) and transmission (T) coefficients can be readily obtained,

$$R = \left| \frac{2(z^2-1)\sin(\omega n d/c)}{(z-1)^2 e^{i\omega n d/c} - (z+1)^2 e^{-i\omega n d/c}} \right|^2,$$
$$T = \left| \frac{4z}{(z-1)^2 e^{i\omega n d/c} - (z+1)^2 e^{-i\omega n d/c}} \right|^2, \tag{55}$$

where

$$n(\omega) = \sqrt{\mu(\omega)\varepsilon(\omega)}, \tag{56}$$

$$z(\omega) = \sqrt{\mu(\omega)/\varepsilon(\omega)}. \tag{57}$$

We consider a slab width of $d = 1.885$ cm composed of PE11BL ferrite, which is modeled by the two-term Lorentzian model given above. Only the permeability is assumed to be dispersive ($\mu_\infty = 1$). A constant permittivity of $\varepsilon = 13$ is assumed. A series of 1D CHICAGO simulations is performed in which an injected TEM wave of a fixed frequency is incident upon a ferrite slab and the reflection and transmission coefficients are calculated. In Fig. 8, the simulation results are plotted along with the theoretical

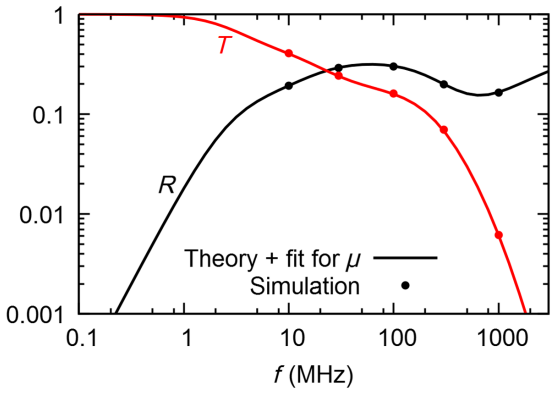

FIG. 8. Reflection (black) and transmission (red) coefficients for an incident transverse wave striking a ferrite slab at normal incidence. The ferrite is modeled using a two-term Lorentzian fit to permeability data for PE11BL. The slab has a width of 1.885 cm. Solid lines show theoretical results using the fitted frequency-dependent permeability. Dots show the simulation results.

results given by Eq. (56). The good agreement for R and T verifies that the dispersion model has been properly implemented. We note that the theoretical results shown in Fig. 8 are calculated using the two-term fit to $\mu(\omega)$ rather than the raw data shown in Fig. 7. The decomposition of the permeability into a linear sum of simple response functions is required by the recursive convolution algorithm used in the simulations. But the raw permeability data can be used in the theory plots shown in Fig. 8. When this is done, there is very little effect on the behavior of R and T over the frequency range shown.

VII. PILLBOX SIMULATIONS IN CHICAGO WITH FERRITES PRESENT

Having demonstrated the capability to perform perpendicular impedance calculations for a simplified pillbox geometry, we now show the effect of adding ferrites into the gap regions. From Eq. (2), it is seen that the BBU growth rate scales linearly with $\mathrm{Re}(Z_\perp)$, so in designing an accelerating gap, it is important to try to reduce that quantity as much as possible. As mentioned above, one method of mitigating BBU is to damp cavity modes of the gap by including lossy ferrites in the gap region. In this section, we present the results for a modified pillbox gap containing the PE11BL ferrite in which the frequency-dependent permeability is modeled by the two-term Lorentzian fit described above (see Fig. 7), along with a constant permittivity, $\varepsilon = 12$.

We consider again a pillbox cavity with beam pipe radius, $b = 7.5$ cm, gap width $d = 3.5$ cm, and $R = 30$ cm. The gap is now terminated by a perfect conductor at $r = R$, i.e., $Z_s/Z_o = 0$. The numerical grid is given by $\Delta r = \Delta z = 0.25$ cm, and $\Delta\theta = \pi/10$. This test problem was motivated by calculations and measurements performed by Dighe at LANL [28]. Dighe calculated perpendicular impedance for a similar test problem using a 3D frequency-domain code and compared the results with experiments from a test cell. The geometry of our 3D cylindrical simulation domain is shown in Fig. 9. The plot on the left shows the gap structure as a function of r and z at $\theta = 0$. There is a PE11BL ferrite wedge with an equilateral triangular cross-section with a width and length of about 1 inch, located at a radius of about 20 cm (shown in red in the figure). The azimuthal structure of the ferrites is shown on the right-hand side of Fig. 9 (cross sections at $z = 3$ cm). In one case (top), we consider a fully axisymmetric ferrite ring and also a case in which there are azimuthal breaks in the ferrite near $\theta = 0$ and π (the simulation geometry is symmetric about $x = 0$). Codes such as AMOS assume an axisymmetric gap geometry and cannot account for such effects.

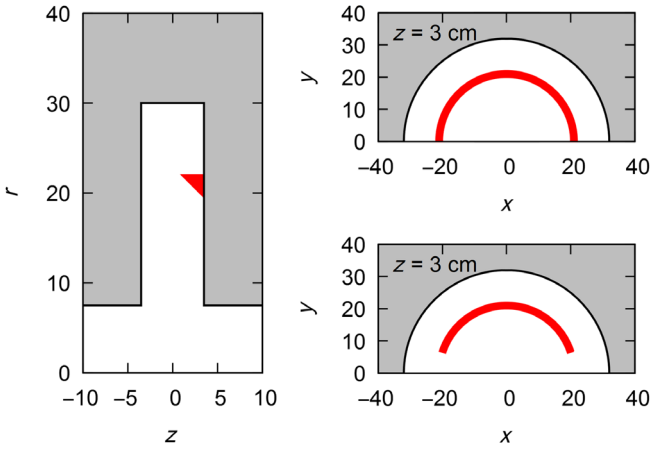

FIG. 9. Simulation geometry of shorted pillbox gap with the addition of a ferrite (shown in red). Left: cross section of gap geometry at $x = 0$ ($\theta = \pi/2$). Cross sections at $z = 3$ cm of (top right) axisymmetric ferrite ring. Bottom right: discrete ferrite arc.

The resulting plots of $Z_\perp$ as a function of frequency are shown in Fig. 10. The black trace shows $Z_\perp$ for the axisymmetric ferrite case. For the case shown in the bottom right of Fig. 9, the results depend on whether the beam is offset in the horizontal (x) or vertical (y) direction, with results from both cases shown in red and blue traces, respectively, in Fig. 10. We note that $Z_\perp$ for the vertical offset with the ferrite arcs is nearly identical to the axisymmetric ferrite case, while there is considerably less damping for the horizontal offset in the case with the ferrite arcs. This can be explained as follows: For a small horizontal offset, the main components of the TM_{1n0} modes, E_z and H_ϕ, have an azimuthal dependence of $\sim\cos\phi$. This implies that fields are largest precisely in the azimuthal regions where the ferrites are absent. This results in diminished damping of the cavity modes. For a small vertical offset, the azimuthal dependence is $\sim\sin\phi$ so that the ferrites are located optimally to damp the fields. Moreover, the ferrites are only absent in the locations where the fields are weakest. For this reason, the vertical offset case is nearly the same as the axisymmetric case.

These results are qualitatively similar and in relatively good quantitative agreement with the results of Dighe [28].

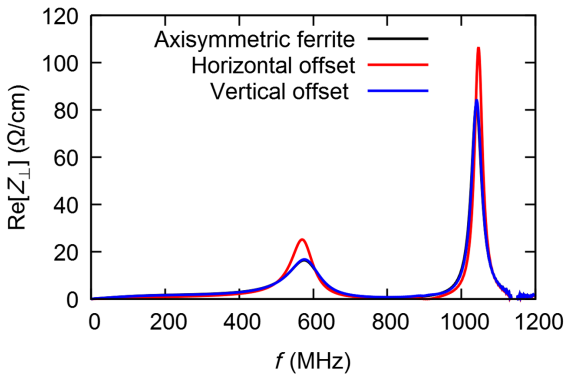

FIG. 10. $Z_\perp$ as a function of frequency for pillbox with ferrite. Black: axisymmetric ferrite ring. Red: ferrite arc with horizontal (x) offset of the beam, and Blue: vertical (y) offset.

But we are unable to directly compare results due to an omission of some geometric data in Dighe's report, specifically, the angle and radial location of the ferrite wedge. The peak values and widths of the BBU resonances are quite sensitive to such parameters.

VIII. SIMULATION RESULTS FOR ETA-II ACCELERATING GAP

As a further illustration of the method, we will consider the perpendicular impedance of the cell for the ETA-II accelerator which is described by DeFord, *et al.* [12]. The geometry of the cell is shown in Fig. 1 of Ref. [12] and is axisymmetric except for the presence of two pulsed-power feeds separated by 180° azimuthally. DeFord simulates this cell in the 2D AMOS code by neglecting the pulsed-power feeds and we retain this approximation. Our approximate axisymmetric cell geometry is shown in Fig. 11. We have also neglected some fine detail in the geometry (compare with Fig. 1 of Ref. [12]).

The ferrite (shown in red) is again taken to be PE11BL, with the permeability modeled by the two-term fit shown in Fig. 7 and a constant real permittivity of 13. This is the same fit used in Ref. [12]. The oil (shown in yellow) is modeled as a dielectric with a permittivity of 2.23 and the alumina with a permittivity of 10.

The numerical grid is given by $\Delta r = \Delta z = 0.05$ cm, and $\Delta\theta = \pi/10$, and a time step of $c\Delta t = \Delta r$ is used. The resulting frequency-dependent $Z_\perp$ is plotted in Fig. 12. Results from the AMOS code, taken from Ref. [12], are shown in black, and the CHICAGO simulation results are shown in red. There is generally good agreement between the two codes for this axisymmetric gap geometry. There is some discrepancy between the two codes above 1 GHz (the beam cutoff frequency is ~ 1.3 GHz). This could be due to the effect of a finite L of 60 cm in the CHICAGO simulation, differences in the permittivity used for the oil and alumina, or some minor differences in the approximate geometry in the two codes. It is difficult to sort out these possible sources of discrepancy, as some of the details of the AMOS simulation are not spelled out in Ref. [12].

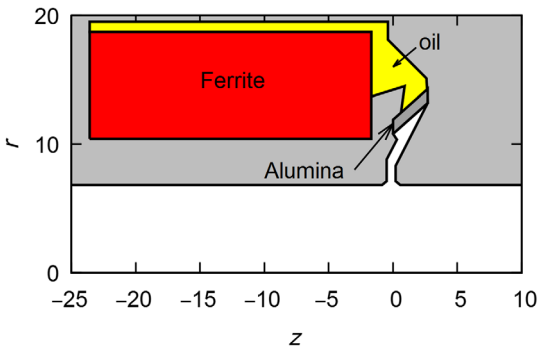

FIG. 11. Simulation geometry of test accelerating gap for ETA-II [12]. Damping ferrite is shown in red. Adapted from Fig. 1 in Ref. [12].

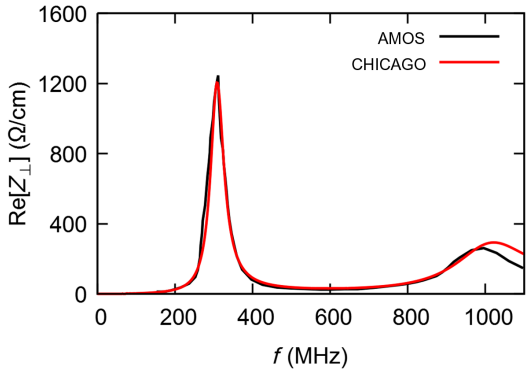

FIG. 12. $Z_\perp$ as a function of frequency for ETA-II cell. Black: AMOS results from Ref. [12]. Red: CHICAGO simulation results.

IX. COMPARISON OF SIMULATION RESULTS WITH EXPERIMENT FOR PERPENDICULAR IMPEDANCE OF SCORPIUS PROTOTYPE TEST CELL

Having verified the models in CHICAGO for calculating $Z_\perp$ for LIA gaps containing damping ferrites, we now calculate the impedance for the PAC test cell, used in testing for the upcoming Scorpius accelerator at the Nevada test site. The PAC has a nonaxisymmetric geometry and is modeled in 3D cylindrical in CHICAGO. The test cell includes eight (oil-filled) induction cells, and three sets of ferrite arcs near the gap are included to dampen the cavity modes. In our model of the PAC, the ferrites are composed of CN20 ferrite. The frequency-dependent permeability of the ferrite materials is plotted in Fig. 13. The solid lines in the figure show the real (black) and imaginary (red) parts of the measured values of the permeability of the ferrite. The dotted lines show the result of fitting the data with a series of weighted Lorentzians (52) and a single Debye response function as described in Sec. V D. Note that by including a sufficient number of response functions,

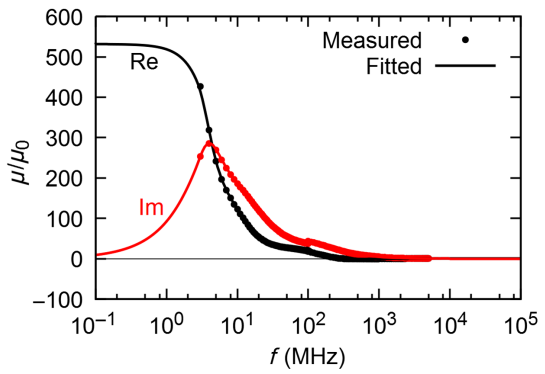

FIG. 13. Permeability data for CN20 ferrite. Measured data shown as dots, solid lines fitted data used in CHICAGO simulation.

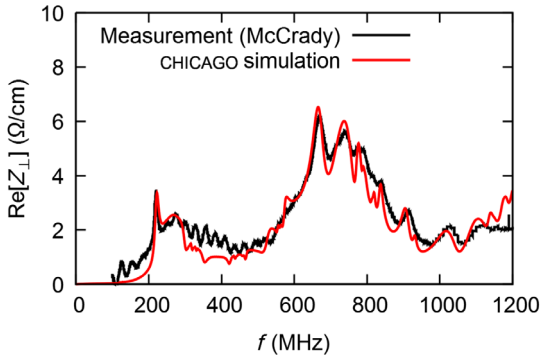

FIG. 14. Comparison of measurement of the perpendicular impedance of PAC test cell to CHICAGO simulation result.

a good wide-band fit to the data can be obtained. The slight discontinuity seen in the imaginary part of μ/μ_0 in Fig. 13 at 100 MHz is an artifact due to the fact that different calibration techniques are used in the measurements above and below this frequency. There is also a frequency band from about 300 MHz to 1.8 GHz in which the real part of μ/μ_0 is negative.

This fitting is used in the CHICAGO simulation to perform the recursive convolution treatment for the ferrite arcs. The permittivity of the ferrites is well approximated by a real frequency-dependent value of $\varepsilon \simeq 13$. The oil-filled cell regions are separated from the beam pipe by a plastic gasket similar to the Alumina gasket shown in Fig. 11.

The CHICAGO simulation is performed with a grid of $\Delta r = \Delta z = 0.25$ cm and $\Delta\theta = \pi/24$. The time step is set by the particle Courant condition, $c\Delta t = \Delta z$. A stiff electron beam of radius 1 cm and horizontal offset of 0.25 cm (one radial cell width) is injected into the beam pipe with a prescribed Gaussian current profile. The perpendicular impedance is calculated from the simulation results by the procedure in Sec. VII. Measurement results were obtained on the PAC at LANL [19]. The comparison between the measurement and the CHICAGO simulation results is shown in Fig. 14, demonstrating good agreement.

X. CONCLUSIONS

We have shown that the parallel and perpendicular impedances of accelerating gaps in LIAs can be calculated numerically from simple PIC simulations in 3D cylindrical coordinates with relatively few azimuthal cells. The use of full 3D coordinates allows for the simulation of a more general class of problems than the restrictions imposed by codes such as AMOS of axisymmetric cell gap geometries. Ferrite materials used to damp cavity resonances are modeled using an implicit field solver in concert with a recursive convolution technique for treating the linear isotropic dispersion of the ferrites. The use of the implicit solver relaxes the usual time step constraints on the simulation, and the time step is restricted only by a particle "Courant" condition in which the beam particles used to seed ($v_z \simeq c$) the cavity modes may not cross a cell longitudinally during a single time step, i.e., $c\Delta t \leq \Delta z$, rather than the more restrictive condition required for a 3D cylindrical grid.

An accurate knowledge of $Z_\perp$ is necessary for designing LIA accelerating gaps as the growth rate of the BBU instability is proportional to this quantity. It is possible, in principle, to model a full LIA entirely with a PIC simulation in which the fully self-consistent interaction of the beam and gap cavities is captured. Modern LIAs such as DARHT [29,30] can be on the order of 50–100 m in length and include hundreds of accelerating cells. Explicitly modeling the entire accelerator length as well as all of the accelerating gaps leads to an extremely large and time-consuming simulation. Another obstacle, perhaps more serious in the near term than a lack of computing resources, to full end-to-end LIA modeling by 3D PIC is the numerical Cherenkov instability (NCI) [31], in which numerical dispersion error of the field solver generates unphysical radiation due to coupling with relativistic PIC particles. In practice, NCI results in nonphysical emittance growth in beam simulations for accelerator segments greater than about 10 m for currents on the order of a kA. For this reason, self-consistent 3D PIC simulations of LIAs on the order of 100 m in length remain challenging. Mitigation of NCI in PIC codes is an active area of research [32,33], however, advances in this area should relax this length constraint.

To circumvent the NCI problem, BBU is studied at present by using codes such as LAMDA. Beam-induced voltage perturbations and centroid deflections are applied to beam disks by incorporating $Z_\parallel$ and $Z_\perp$ gap data. Until a robust solution to NCI can be developed for lengthy LIA simulations, this will likely remain the method of choice for studying BBU and related instabilities. We have here described a new means by which $Z_\parallel$ and $Z_\perp$ can be obtained by modest-sized 3D PIC simulations. We have also demonstrated that the BBU model used by the beam transport code LAMDA gives beam deflections at gap locations which are in good agreement with full PIC simulations over short accelerator segments, for which NCI is sufficiently suppressed.

ACKNOWLEDGMENTS

The authors would very much like to thank Katherine Velas, Saeed Assadi, Brent McHale, Al Churby, Nate Pogue, Andrea Schmidt, Jennifer Ellsworth, and Jim Watson of Lawrence Livermore National Laboratory, and Carl Ekdahl, Rod McCrady, Sergey Kurennoy, and Mark Crawford of Los Alamos National Laboratory, for critical discussions and strong support of this effort. The work was performed under the auspices of the U.S. Department of Energy by Lawrence Livermore National Laboratory under Contract No. DE-AC52-07NA27344.

[1] G. J. Caporaso and Y. J. Chen, Electron induction linacs, in *Induction Accelerators* (Springer-Verlag, Berlin, Germany, 2011), pp. 117–163.

[2] H. Davis and R. Scarpetti, Modern electron induction LINACs, in *Proceedings of the 23rd International Linac Conference, LINAC-2006, Knoxville, TN, 2006*, (JACoW, Knoxville, TN, 2006), https://accelconf.web.cern.ch/l06/PAPERS/TU1003.PDF.

[3] W. K. H. Panofsky and M. Bander, Asymptotic theory of beam break up in linear accelerators, Rev. Sci. Instrum. **39**, 206 (1968).

[4] V. K. Neil, Laurence S. Hall, and R. K. Cooper. Further theoretical studies of the beam breakup instability, Part. Accel. **9**, 213 (1979), http://cds.cern.ch/record/1107964/files/p213.pdf.

[5] Y. Y. Lau, Classification of Beam Breakup Instabilities in Linear Accelerators, Phys. Rev. Lett. **63**, 1141 (1989).

[6] R. J. Briggs, D. L. Birx, G. J. Caparaso, V. K. Neil, and T. C. Genoni, Theoretical and experimental investigation of the interaction impedances and Q values of the accelerating cells in the advanced test accelerator, Part. Accel. **18**, 41 (1985), https://cds.cern.ch/record/1108029/files/p41.pdf.

[7] J. E. Coleman, C. A. Ekdahl, D. C. Moir, G. W. Sullivan, and M. T. Crawford, Correcting the beam centroid motion in an induction accelerator and reducing the beam breakup instability, Phys. Rev. ST Accel. Beams **17**, 092802 (2014).

[8] C. Ekdahl, *et al.*, Long-pulse beam stability experiments on the DARHT–II linear induction accelerator, IEEE Trans. Plasma Sci. **34**, 460 (2006).

[9] R. Briggs, D. Birx, S. Nelson, L. Reginato, and M. Vella, Transverse impedance measurements of the DARHT-2 accelerator cell, in *Proceedings of the Particle Accelerator Conference, Chicago, IL, 2001* (IEEE, New York, 2001), https://accelconf.web.cern.ch/p01/PAPERS/TPPH079.PDF.

[10] T. P. Hughes, C. B. Mostrom, T. C. Genoni, and C. Thoma. LAMDA user's manual and reference, Voss Scientific, LLC, Technical Report No. VSL-0707, 2007.

[11] Carl Ekdahl, Joshua E. Coleman, and Brian Trent McCuistian, Beam breakup in an advanced linear induction accelerator, IEEE Trans. Plasma Sci. **44**, 1094 (2016).

[12] J. F. DeFord, G. Kamin, G. D. Craig, and L. Walling, Dispersive soft ferrite models for time-domain simulation and their application to accelerator component modeling, Part. Accel. **45**, 135 (1994), https://cds.cern.ch/record/1108292/files/p135.pdf.

[13] J. F. DeFord, G. D. Craig, and R. McLeod, The AMOS (azimuthal mode simulator) code, in *Proceedings of the 1989 Particle Accelerator Conference, Chicago, IL* (IEEE, New York, 1989), Vol. 2, pp. 1181–1183.

[14] C. Thoma, D. R. Welch, R. E. Clark, D. V. Rose, and I. E. Golovkin. Hybrid-PIC modeling of laser-plasma interactions and hot electron generation in gold hohlraum walls. Phys. Plasmas **24**, 062707 (2017).

[15] (https://www.vosssci.com/products/chicago/chicago.html).

[16] A. Taflove, *Computational Electrodynamics: The Finite-Difference Time-Domain Method* (Artech House, Inc., Washington, DC, 1995).

[17] R. J. Luebbers and F. Hunsberger, FDTD for Nth-order dispersive media, IEEE Trans. Antennas Propag. **40**, 1297 (1992).

[18] R. J. Luebbers, J. D. Steich, and K. Kunz, FDTD calculation of scattering from frequency-dependent materials, IEEE Trans. Antennas Propag. **41**, 1249 (1993).

[19] C. Ekdahl, S. Kurennoy, R. McCrady, and G. Dale, Beam breakup simulations for the Scorpius flash-radiography accelerator, IEEE Trans. Plasma Sci. **50**, 684 (2022).

[20] Mark Crawford and Juan Barraza, Scorpius: The development of a new multi-pulse radiographic system, in *Proceedings of 2017 IEEE 21st International Conference on Pulsed Power (PPC), Brighton, UK* (IEEE, New York, 2017), pp. 1–6.

[21] J. F. DeFord, G. D. Craig, and R. R. McLeod, The AMOS wakefield code, LLNL, Technical Report No. UCRL-102731, 1990.

[22] J.-P. Berenger, Perfectly matched layer for the FDTD solution of wave-structure interaction problems, IEEE Trans. Antennas Propag. **44**, 110 (1996).

[23] S. D. Gedney, An anisotropic perfectly matched layer-absorbing medium for the truncation of FDTD lattices, IEEE Trans. Antennas Propag. **44**, 1630 (1996).

[24] J. Alan Roden and Stephen D. Gedney, Convolution PML (CPML): An efficient FDTD implementation of the CFS–PML for arbitrary media, Microwave Opt. Technol. Lett. **27**, 334 (2000).

[25] M. Reiser, *Theory and Design of Charged Particle Beams* (John Wiley and Sons, New York, 1994).

[26] B. B. Godfrey, Time-biased field solver for electromagnetic PIC codes, in *Proceedings of the 9th Conference on Numerical Simulation of Plasmas, Washington, DC* (Northwestern University, Evanston, IL, 1980).

[27] B. B. Godfrey and B. C. Goplen, Practical evaluation of time-biased electromagnetic-field algorithms for plasma simulations, Bull. Am. Phys. Soc. **25**, 854 (1980).

[28] K. A. Dighe, Determination of transverse impedance of Scorpius LIA test cell, LANL, Technical Report No. LA-UR-19-23738, 2019.

[29] C. Ekdahl, Modern electron accelerators for radiography, in *PPPS-2001 Pulsed Power Plasma Science 2001. 28th IEEE International Conference on Plasma Science and 13th IEEE International Pulsed Power Conference. Digest of Papers (Cat. No.01CH37251), Las Vegas, NV* (IEEE, New York, 2002), Vol. 1, pp. 29–34.

[30] K. Peach and C. Ekdahl, Particle beam radiography, Rev. Accel. Sci. Technol. **06**, 117 (2013).

[31] B. B. Godfrey, Numerical Cherenkov instabilities in electromagenetic particle codes, J. Comput. Phys. **15**, 504 (1974).

[32] J.-L. Vay, C. G. R. Geddes, E. Cormier-Michel, and D. P. Grote, Numerical methods for instability mitigation in the modeling of laser wakefield accelerators in a Lorentz-boosted frame, J. Comput. Phys. **230**, 5908 (2011).

[33] X. Xu, P. Yu, S. F. Martins, F. S. Tsung, V. K. Decyk, J. Vieira, R. A. Fonseca, W. Lu, L. O. Silva, and W. B. Mori, Numerical instability due to relativistic plasma drift in EM-PIC simulations, Comput. Phys. Commun. **184**, 2503 (2013).